ACCSCIENCE PUBLISHING

International Journal of Bioprinting

RESEARCH ARTICLE

Multiscale vascularized tumor-on-a-chip via bioprinting for drug research

Jing Liu[1], Ying Zhao[1], Bihan Ren[1], Dingming Li[1], Tianma He[1], Haizhongshi Zhang[1], Zhenlei Zhang[1], and Haochen Liu[2]*

[1]Department of Biological Engineering, School of Biology, Food and Environment, Hefei University, Hefei, Anhui, China

[2]Department of Cardiovascular Surgery, Xi'an Children's Hospital, Xi'an, Shaanxi, China

Abstract

Current *in vitro* tumor models often fail to recapitulate the hierarchical vascular architecture and dynamic interactions of the tumor microenvironment (TME), limiting their utility in cancer research. In this study, we present a multiscale vascularized tumor model integrating coaxial bioprinting, inkjet printing, and fused deposition modeling (FDM) to address this challenge. Firstly, coaxial bioprinting enabled the fabrication of dual-layered vasculature with an endothelium layer and a smooth muscle layer. Secondly, tumor spheroids with precise size control (±10 μm) were generated via inkjet printing by modulating Methacrylate Gelatin (GelMA) concentration and valve actuation time. An FDM-printed chip was designed to co-culture these components under perfusion, facilitating the self-organization of a microvascular network around tumor spheroids. After 11 days of dynamic culture, the model demonstrated tumor-driven angiogenic sprouting and early metastatic behavior, validated by the upregulation of metastasis-related genes (CD44, MMP2, N-cadherin) in vascularized cohorts. Drug testing with paclitaxel revealed dose-dependent suppression of tumor proliferation and invasion. This platform not only mimics the structural and functional complexity of the TME but also provides a scalable, physiologically relevant tool for investigating tumor–vascular crosstalk and evaluating anti-cancer therapeutics.

Keywords: 3D bioprinting; Coaxial printing; Drug research; Inkjet printing; Tumor-on-a-chip; Vascularized tumor model

***Corresponding author:**
Haochen Liu
(haochen1010@163.com)

Citation: Liu J, Zhao Y, Ren B, *et al.* Multiscale vascularized tumor-on-a-chip via bioprinting for drug research. *Int J Bioprint.* 2025;11(4):378-391. doi: 10.36922/IJB025180180

Received: May 1, 2025
1st revised: June 11, 2025
2nd revised: June 24, 2025
3rd revised: June 26, 2025
Accepted: June 26, 2025
Published online: June 26, 2025

1. Introduction

Cancer is currently the second leading cause of death worldwide, following cardiovascular diseases. According to the World Health Organization, nearly 10 million cancer-related deaths were reported globally in 2022, accounting for one-sixth of total mortality, with a rising prevalence in underdeveloped regions.[1] Despite significant advances in cancer research, the molecular mechanisms underlying tumorigenesis and progression remain poorly understood, contributing to the high failure rate and exorbitant costs of anti-cancer drug development.[2] A major challenge lies in the lack of *in vitro* models that accurately replicate the human tumor microenvironment (TME), leading to discrepancies between preclinical drug testing and clinical outcomes.[3] The TME is a highly dynamic ecosystem,

comprising tumor cells, stromal cells, vascular networks, and the extracellular matrix (ECM), where intricate interactions govern tumor progression, drug penetration, and therapeutic response.[4] Thus, the development of *in vitro* tumor models that integrate multiscale vascular networks and recapitulate TME dynamics is essential to overcoming current research bottlenecks.

Traditional 2D cell models, though simple and suitable for high-throughput screening, fail to replicate the 3D cell–cell interactions, metabolic gradients, and drug diffusion barriers of solid tumors.[5,6] Animal models, while capable of mimicking *in vivo* tumor environments, face limitations due to high costs, species-specific discrepancies, and ethical concerns.[7] In contrast, 3D tumor models better approximate the TME by simulating spatial cell arrangements, heterogeneity, and ECM physicochemical properties.[8] At present, tumor spheroid-based models are the primary focus of 3D tumor models. These models, resembling human tumors in morphology, high cell density, and chemical environment, effectively establish physiological metabolic gradients.[9] Furthermore, these models are often integrated with tumor cells and fibroblasts. The latter, by secreting angiogenic factors such as vascular endothelial growth factor (VEGF), plays an essential role in tumor growth, invasion, metastasis, and angiogenesis.[10–12] The fabrication of tumor spheroids primarily relies on traditional techniques, including ultra-low adhesion methods,[13] hanging drop techniques,[14–16] and droplet overlay methods.[17–19] While these approaches are simple to operate, they exhibit significant limitations; for instance, they lack precise control over spheroid diameter.[20–22] Furthermore, most current studies are restricted to monoculture systems of tumor cells, failing to systematically integrate key functional units of the TME, such as perfusable vascular networks and immune cell infiltration.[23–25]

Blood vessels, as pivotal functional units of the TME, not only deliver oxygen and nutrients but also regulate immune cell infiltration and drug delivery.[26] Native vasculature features a complex tri-layered structure (intima, media, adventitia), where endothelial and smooth muscle cells synergistically maintain vascular tone, barrier function, and paracrine signaling.[27–30] Existing *in vitro* vascular models, however, primarily rely on endothelial-lined hollow channels, which neither mimic layered vascular structures nor support long-term perfusion.[31–35] While 3D bioprinting offers new avenues for constructing spatially controlled vascularized models, integrating multiscale vascular networks (from macrovessels to capillaries) with tumor spheroids remains technically challenging.[36] In this study, we present an innovative multiscale vascularized tumor model developed through the integration of coaxial bioprinting, inkjet printing, and fused deposition modeling (FDM). Notably, coaxial bioprinting enabled the fabrication of dual-layered vascular constructs featuring endothelial and smooth muscle layers, a design strategy aimed at mimicking native vascular architecture. Concurrently, inkjet printing achieved high-precision tumor spheroid generation (±10 μm dimensional consistency), effectively addressing the heterogeneity limitations inherent in conventional spheroid formation techniques. The FDM-fabricated perfusion culture chip further advanced the system's functionality by facilitating dynamic tumor–vascular co-culture and enabling real-time microenvironment monitoring. Preliminary mechanistic investigations leveraging this integrated platform revealed insights into paclitaxel-mediated suppression of tumor metastasis. Collectively, this model successfully simulated tumor-associated vascular radial growth, early metastatic events, and drug responses, providing a robust platform for investigating tumor–vascular interactions and evaluating anti-angiogenic therapies.

2. Materials and methods

2.1. Materials

Human fetal lung fibroblast 1 (HFL1; CCL-153), human umbilical vein endothelial cells (HUVECs; CRL-1730), human aortic vascular smooth muscle cells (HA-VSMCs; CRL-1999), and human hepatocellular carcinoma G2 (HepG2; HB-8065) were purchased from the American Type Culture Collection (ATCC, United States of America [USA]). Dulbecco's Modified Eagle Medium (DMEM), 0.25% Trypsin-EDTA, and phosphate-buffered saline (PBS) were obtained from Wuhan Servicebio Technology Co., Ltd. (China). Fetal bovine serum (FBS) was sourced from Lonsa Sience SRL (Uruguay). Penicillin-streptomycin was purchased from Gibco (USA). Anhydrous calcium chloride, propidium iodide (PI), DiO (green cell membrane fluorescent probe), DiI (orange cell membrane fluorescent probe), 4% paraformaldehyde, Triton X-100, gelatin (bloom number: 240~270), and bovine serum albumin (BSA) were obtained from Sangon Biotech Co., Ltd. (China). Lithium phenyl-2,4,6-trimethylbenzoylphosphinate (LAP), fibronectin, methacrylic anhydride, and Calcein-AM were obtained from Shanghai Aladdin Biochemical Technology Co., Ltd. (China). Pluronic F-127, Phalloidin-FITC, alginate, and fibrinogen were purchased from Sigma-Aldrich Corporation (USA). Thrombin was obtained from Yeasen Biotech Co., Ltd. (China). Total RNA extraction commercial kit, reverse transcription kit, and 2× Universal Blue SYBR Green qPCR Master Mix were obtained from Mei5 Biotechnology (China). Gelatin methacryloyl (GelMA) and type I rat tail collagen were synthesized in-house. Anti-CD31 antibody (152 μg/mL) was obtained

from Cell Signaling Technology (USA), and Alexa Fluor 568 donkey anti-rabbit IgG (H+L) (2 mg/mL) was obtained from Thermo Fisher (USA).

2.2. Cell culture

The cells (HFL1, HUVECs, HA-VSMCs, and HepG2) were maintained in high-glucose DMEM medium supplemented with 10% (v/v) FBS and 1% (v/v) penicillin-streptomycin at 37 °C in a humidified incubator (STIK, China) with 5% CO_2. When the cells reached 90% confluence, they were passaged at an appropriate ratio using 0.25% Trypsin-EDTA. The culture medium was refreshed every 2–3 days.

2.3. Preparation of type I collagen

The skin of the rat tail was removed to extract the silver-colored tendons, which were washed thoroughly and blotted dry. After cutting the tendons into small pieces, they were immersed in 0.1% acetic acid for 7 days. The solution was centrifuged at 8000 rpm (6738 × *g*) for 30 min, and the supernatant was collected and freeze-dried. The lyophilized collagen was weighed and dissolved in 0.1% acetic acid supplemented with 1% penicillin-streptomycin to prepare a 10% collagen solution, which was stored at 4°C.

2.4. Preparation of GelMA

Gelatin was dissolved in PBS and heated at 50 °C for 2 h until fully dissolved. The solution was stirred on a magnetic stirrer, and methacrylic anhydride (MA) was added dropwise for a complete reaction. The reaction mixture was centrifuged at 4500 rpm (2132 × *g*) for 10 min, after which the supernatant was dialyzed in distilled water at 37°C for 7 days, and the dialyzed solution was subsequently freeze-dried. Both GelMA and the original gelatin were characterized by 1H-NMR (Figure S1, Supporting Information), demonstrating the successful synthesis of GelMA (30–50% substitution rate).[37] The resulting GelMA was dissolved in sterile complete medium to prepare a 14% solution, which was stored at 4°C.

2.5. Fabrication of bilayered vessels

2.5.1. Bioink preparation

The outer shell bioink consisted of HA-VSMCs embedded in a matrix containing 8 mg/mL rat tail collagen, 1% (w/v) sodium alginate, 0.25% (w/v) LAP, and 3% (w/v) GelMA. The inner sacrificial ink was a thermosensitive composite composed of 3% (w/v) $CaCl_2$ and 4% (w/v) Pluronic F-127. Crosslinking of the outer shell bioink was achieved through ionic gelation by Ca^{2+}, while Pluronic F-127 served as a temporary scaffold to maintain the hollow structure during printing. Notably, rat tail collagen must be neutralized to physiological pH with NaOH under ice-bath conditions, and the mixing of the outer shell bioink should also be performed at 4 °C. The internal sacrificial ink needs to be pre-dissolved at 4 °C in advance. The entire operation process is strictly carried out in compliance with aseptic operation specifications.

2.5.2. Printing and post-processing

Coaxial extrusion-based printing was performed using a 20G/25G nozzle, with flow rates of 2.5 and 3.0 mL/min for the outer and inner inks, respectively. The printed tubular structures were immersed in 2% $CaCl_2$ solution for 2 min to induce ionic crosslinking, rinsed with PBS, and then photocrosslinked under 405 nm light for 30 s. Subsequently, fibronectin (1 mg/mL) was infused into the lumen via a sterile syringe and incubated dynamically at 37 °C for 15 min, with inversion every 5 min. HUVECs suspended in 2 mg/mL collagen (1×10^6 cells/mL) were then loaded into the lumen in two steps, 12 h apart, with rotation to ensure uniform endothelial coverage. All procedures were conducted under sterile conditions.

2.6. Tumor spheroid formation

Tumor spheroids were fabricated via inkjet bioprinting. A bioink was prepared by mixing a cell suspension containing HepG2 (6×10^7 cells/mL) and HFL1 (2×10^7 cells/mL) at a 3:1 ratio of HepG2/HFL1,[4,9] with a base ink containing 10% (w/v) GelMA and 0.5% (w/v) LAP at a 1:1 ratio. Optimized printing parameters (e.g., pressure, valve timing, and viscosity) were applied to generate uniform droplets at 37°C. The printed microspheres were deposited onto low-attachment culture dishes and crosslinked under 405 nm light for 30 s to obtain tumor spheroids with controlled diameters.

2.7. Chip design and fabrication

A custom-designed microfluidic culture chip was fabricated using polylactic acid (PLA) via FDM. The chip featured a central channel (diameter: 2 mm) for embedding the bilayered vascular construct, and four radial culture chambers for establishing a vascularized TME. The PLA chip was bonded to a glass slide using medical-grade adhesive and sealed with a coverslip to form a closed culture system (Figure 1). Regarding the disinfection of the culture system, it is worth noting that all autoclave-tolerant components (silicone tubing, stainless-steel connectors) were sterilized via autoclaving at 121°C for 30 min. For non-autoclavable FDM-printed chips (disposable products), a sequential protocol was implemented as follows: immersion in 75% ethanol for 30 min, thorough rinsing with PBS, and UV treatment for 30 min.

2.8. Construction of the multiscale vascularized tumor model

The bilayered vessel was positioned in the central channel and connected to a perfusion loop using silicone tubing (inner diameter: 1 mm). A pre-chilled matrix, which was

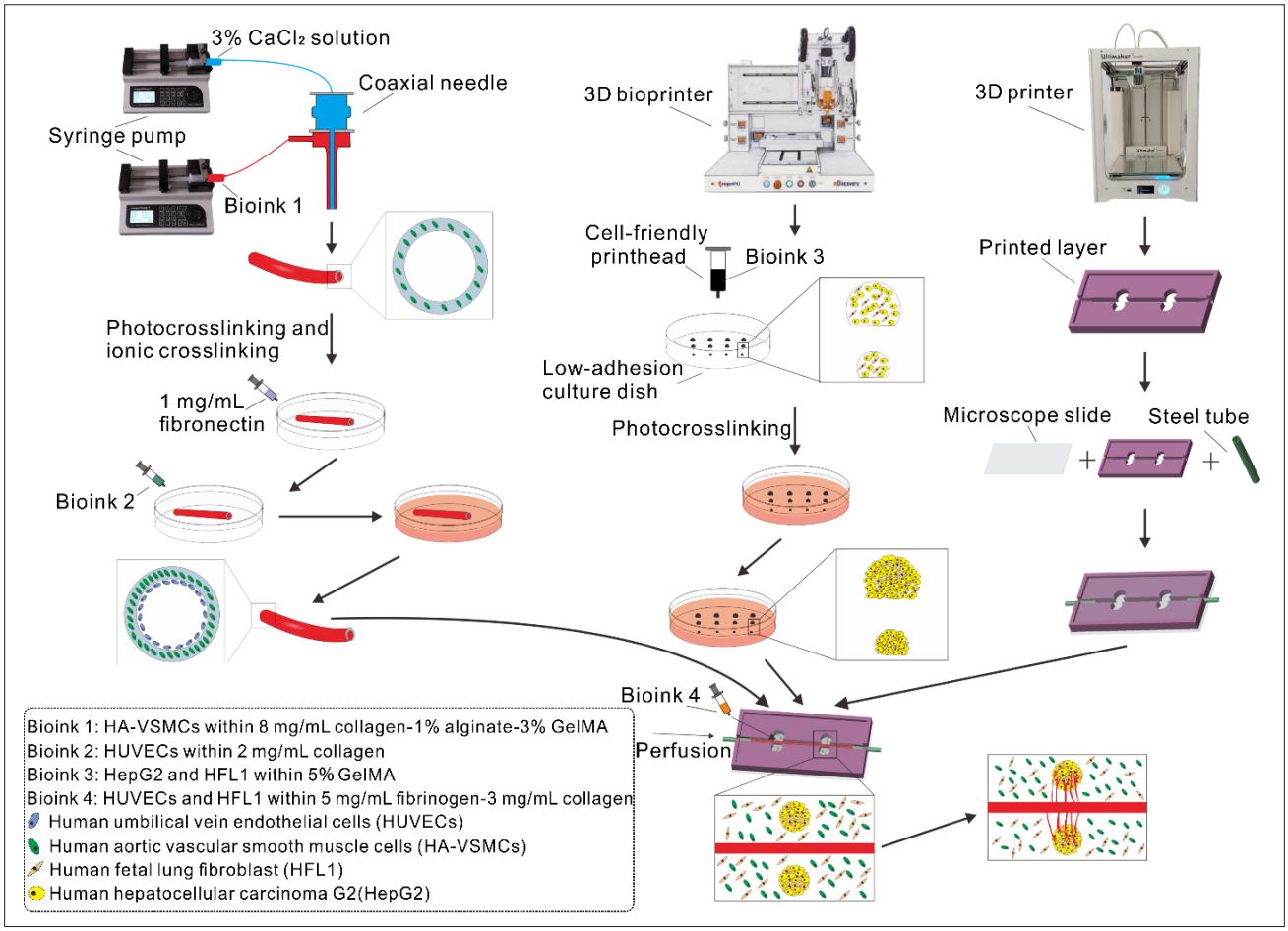

Figure 1. Preparation of an *in vitro* tumor model.

formulated with 10 mg/mL fibrinogen and 6 mg/mL type I collagen, was prepared. This matrix was then mixed in a 1:1 ratio with a solution containing HUVECs (2×10^6 cells/mL), HFL1 (1×10^6 cells/mL), tumor spheroids, and 10 U/mL thrombin. The mixture was injected into the chip chambers and allowed to gel at 37 °C for 15 min. Continuous perfusion culture was initiated using a peristaltic pump (BT100-2J; LongerPump, China) at a flow rate of 50 μL/min to mimic physiological conditions.

2.9. Live/dead cell staining

Cell viability was assessed using Calcein-AM/PI staining. Calcein-AM (5 μM) and PI (10 μg/mL) were added to the culture system and incubated at 37 °C and 5% CO_2 for 30 min. Samples were washed three times with PBS to remove excess dye. Fluorescence images were captured using a high-content imaging system (CQ1; Yokogawa, Japan) with excitation wavelengths of 488 nm (Calcein-AM) and 561 nm (PI). ImageJ was used to quantify fluorescence intensity and calculate the ratio of viable cells.

2.10. Spheroid monitoring

HepG2 and HFL1 were labeled with DiO (green) and DiI (red) fluorescent dyes, respectively, and then used to prepare tumor spheroids as described. The CQ1 imaging system was used to observe and record spheroid morphology on Days 1, 3, and 7.

2.11. Immunofluorescence staining

Samples were fixed with 4% paraformaldehyde for 10–20 min, permeabilized with 0.1% Triton X-100 for 5–10 min at room temperature, and washed with PBS. After blocking with 5% BSA for 30 min, samples were incubated with primary antibodies overnight at 4 °C or for 1–2 h at room temperature. After PBS washes, fluorescently labeled secondary antibodies were applied for 1 h in the dark. The final concentrations of the antibodies were as follows: anti-CD31 antibody at 152 ng/mL, and Alexa Fluor 568 donkey

anti-rabbit IgG at 4 μg/mL. Staining results were imaged using the CQ1 fluorescence microscope to analyze protein expression and localization.

2.12. Cytoskeleton staining

Fixed and permeabilized samples were stained with Phalloidin-FITC (10 μg/mL) in the dark at room temperature for 1 h. After three washes with PBST (0.1% Triton X-100 in PBS, pH 7.4), samples were imaged using the CQ1 system under 488 nm excitation to visualize cytoskeletal structures.

2.13. Quantitative reverse transcription polymerase chain reaction

Gene expression was analyzed by quantitative reverse transcription polymerase chain reaction (qRT-PCR). Total RNA was extracted using a commercial kit following the manufacturer's instructions. RNA concentration and purity were assessed using a microvolume spectrophotometer (LB 915; Colibri, Germany). Complementary DNA (cDNA) was synthesized from RNA using a commercial reverse transcription kit. SYBR Green-based qRT-PCR (Roche, Switzerland) was performed using primers listed in **Table 1**. Gene expression was normalized to glyceraldehyde-3-phosphate dehydrogenase (GAPDH) and analyzed using the $2^{-\Delta\Delta Ct}$ method.

2.14. Statistical analysis

Quantitative data are presented as mean ± standard deviation (SD) for at least three samples per test ($n \geq 3$). Prior to statistical testing, all datasets were assessed for normality using the Shapiro-Wilk test. Only data conforming to a normal distribution were subjected to parametric analysis. The p-values were calculated via a two-tailed Student's t-test for comparisons between two groups or one-way analysis of variance (ANOVA) for multiple group comparisons. Significance levels are indicated as * for $p < 0.05$, ** for $p < 0.01$, *** for $p < 0.001$, and N.S. for no significant difference.

3. Results and discussion

3.1. Fabrication of hollow tubes using a coaxial nozzle

To achieve a balance between the mechanical properties and biocompatibility of the hollow tubes, we systematically investigated the formulation of alginate, collagen, and GelMA in the bioink. As displayed in Figure 2A, under a fixed GelMA concentration of 3% (w/v), stable hollow tube formation was achieved when the alginate concentration ranged from 1% to 1.5% (w/v) and collagen was maintained at 5 mg/mL. However, this formulation exhibited limited biocompatibility and failed to support the formation of a dense endothelial layer. Through further optimization, we found that increasing the collagen concentration to 8 mg/mL while maintaining alginate at 1% (w/v) resulted in a composite bioink (3% GelMA, 1% alginate, and 8 mg/mL collagen) with the best overall performance in terms of printability, structural integrity, and cellular compatibility. Unlike coaxial strategies relying on homogeneous bioinks,[38,39] our approach achieves dual-layered microvessels with physiological mechanical properties and sustained cell viability. To meet the requirements for constructing multiscale vascular networks, we further

Table 1. Primer sequences

Gene	Primer sequence (5'–3')	
	Forward	Reverse
GAPDH	ACAACTTTGGTATCGTGGAAGG	GCCATCACGCCACAGTTTC
CD40	GCTTCTTCTCCAATCAGTCAT	ACCTCCAAGTTCTTATCCTCA
Casp-4	CTACGATGTGGTGGTGAA	TGATGTCTGGTGTTCTGAG
CD44	AGAAGGTGTGGGCAGAAGAA	AAATGCACCATTTCCTGAGA
CD70	TGCTGCTGGTGGTGTTTA	CCTCTGTTGCTGCTTACTGA
CD133	GGCCCAGTACAACACTACCAA	ATTCCGCCTCCTAGCACTGAA
CXCL12	TGCCAGAGCCAACGTCAAG	CAGCCGGGCTACAATCTGAA
CXCR4	TGACGGACAAGTACAGGCTGC	CCAGAAGGGAAGCGTGATGA
Fas	GTTGTTGACCATCCTTGTT	TCACGACTGGAGGTTCTA
MMP2	GTGCTGAAGGACACACTAAAGAAGA	TTGCCATCCTTCTCAAAGTTGTAGG
MMP9	AGACCTGGGCAGATTCCAAAC	CGGCAAGTCTTCCGAGTAGT
N-cadherin	AGCCAACCTTAACTGAGGAGT	GGCAAGTTGATTGGAGGGATG
Tnfrsf11b	AGAGTGAGGCAGGCTATT	TGAGGAGAGGAAGGAAGG

adjusted the inner and outer diameters, as well as the wall thickness, of the hollow tubes by switching coaxial needle sizes (Figure 2B). The mechanical properties of the printed hollow tubes were evaluated using a universal testing machine. As displayed in Figure 2C, the tubes exhibited a tensile strain of approximately 23% and a tensile stress of about 0.54 MPa, closely matching the mechanical characteristics of native small-diameter vessels, such as rat mesenteric arteries.[40–42] To further verify the structural integrity and permeability of the hollow tubes, we perfused a red dye solution through the lumen. As presented in Figure 2D, the dye rapidly filled the entire tube and then diffused uniformly into the surrounding medium, confirming the tube's permeability. Notably, the structural stability of the printed tubes was reinforced through the synergistic crosslinking of GelMA by 405 nm light and alginate by Ca^{2+} ions. To support optimal growth and proliferation of HA-VSMCs and HUVECs, we sought to maximize the proportion of collagen in the bioink. However, when the collagen concentration exceeded 8 mg/mL, the viscosity of the bioink significantly increased, which hindered the stability of the printing process and the formation of consistent hollow structures.

3.2. Fabrication of double-layered blood vessels

To evaluate the biological activity of the smooth muscle and endothelial layers within the double-layered blood vessels, we employed Calcein-AM/PI dual fluorescence staining to independently assess cell viability in each layer (Figure 3). For the smooth muscle layer, HA-VSMCs were cultured from Day 1 to Day 10, and the results (Figure 3A and B) revealed a pronounced time-dependent increase in cell proliferation. Throughout the culture period, cell viability consistently remained above 90%, indicating robust and

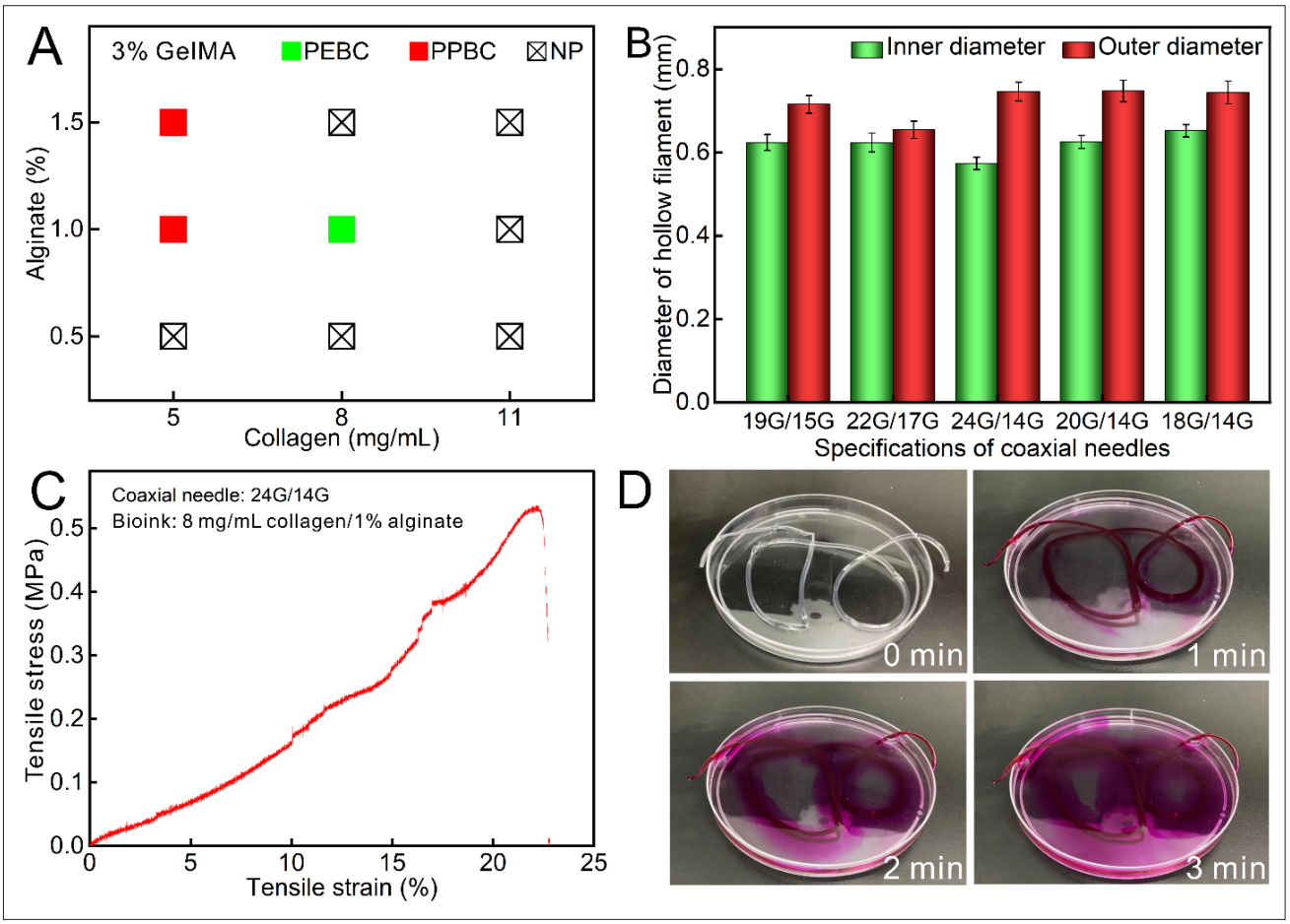

Figure 2. Fabrication and characterization of hollow tubes using coaxial bioprinting. (A) Printability and biocompatibility map of composite bioinks (GelMA, PEBC, PPBC, and NP). (B) Tunable inner and outer diameters of hollow tubes fabricated with different coaxial nozzle configurations. (C) Mechanical properties of hollow tubes. (D) Visualization of tube permeability and diffusivity using perfused red dye. Experiments were independently repeated at least three times ($n \geq 3$). Abbreviations: GelMA, Methacrylate Gelatin; NP, non-printable; PEBC, printable with excellent biocompatibility; PPBC, printable with poor biocompatibility.

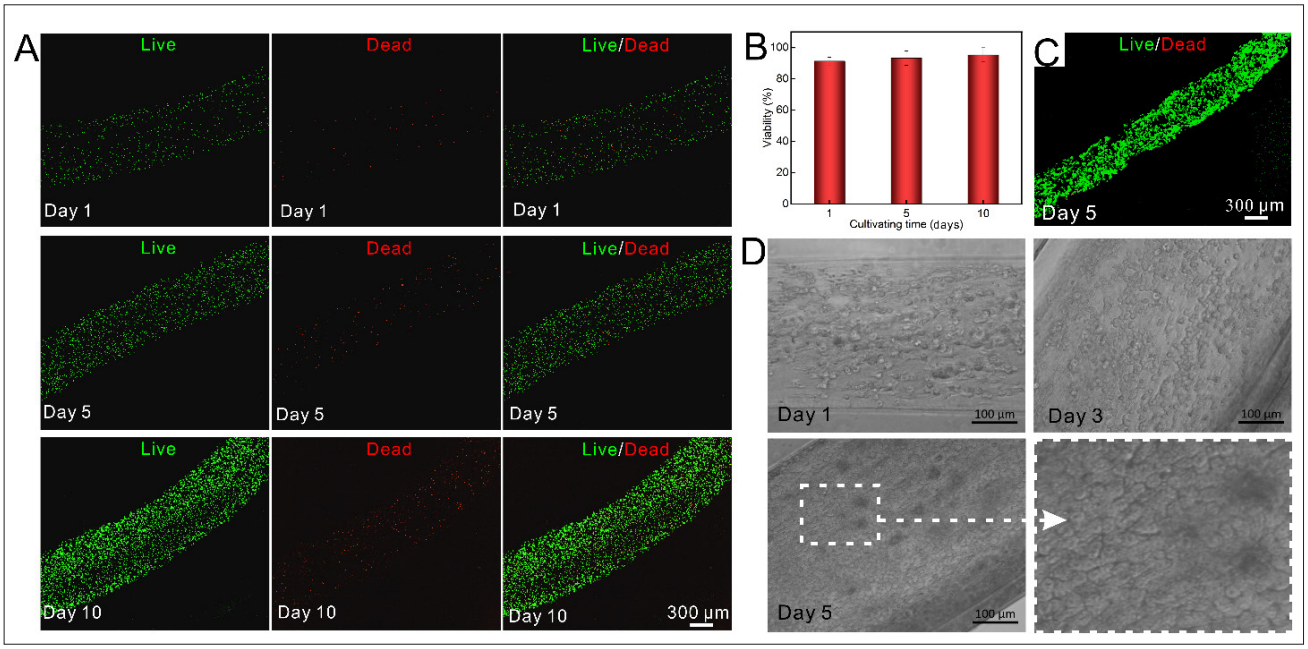

Figure 3. Evaluation of cell viability and morphology in double-layered vascular structures. (A) Temporal evaluation of smooth muscle cell proliferation from Day 1 to Day 10. (B) Quantitative analysis of HA-VSMCs viability embedded in the outer layer of hollow tubes. (C) Live/dead staining of endothelial cells (HUVECs) after 5 days of dynamic perfusion. (D) Formation of a continuous and dense inner monolayer. Experiments were independently repeated at least three times ($n \geq 3$). Scale bars: 300 μm (A and C); 100 μm (D). Abbreviations: HA-VSMCs, human aortic vascular smooth muscle cells; HUVECs, human umbilical vein endothelial cells.

sustained metabolic activity in the smooth muscle layer. For the endothelial layer, HUVECs were subjected to dynamic perfusion for 5 days. As displayed in Figure 3C and D, the cells formed a continuous, densely packed monolayer and maintained high viability (>90%). To enable a more intuitive assessment of morphology and viability, the two cell layers were cultured and stained separately. This strategy demonstrated excellent cell survival and proliferation in both layers. The successful formation of a dense endothelial layer is essential for mimicking the physiological functions of native blood vessels, including molecular exchange, inflammatory response regulation, and barrier protection. These results collectively suggest that the engineered double-layered vessel structure provides a biologically relevant and functional platform, making it highly suitable for downstream drug screening and vascular research applications.[43,44]

3.3. Fabrication and culture of tumor microspheroids

To construct tumor spheroids with precisely controlled dimensions, a high-resolution inkjet bioprinting strategy was innovatively employed in this study (Figure 4A). By tuning the GelMA concentration and the valve opening time of the droplet dispenser, the droplet volume could be precisely regulated. Subsequent crosslinking under 405 nm light enabled the formation of structurally stable tumor spheroids. As displayed in Figure 4B and C, under a fixed GelMA concentration of 5% (w/v), increasing the valve opening time from 200 to 500 μs led to a significant increase in the average spheroid diameter, from 154 to 430 μm. Conversely, when the valve opening time was held constant at 300 μs, increasing the GelMA concentration from 3% to 6% (w/v) raised the solution viscosity, thereby reducing droplet volume and leading to a decrease in spheroid diameter from 293 to 221 μm. This behavior is consistent with a viscosity-dominated droplet breakup mechanism in fluid dynamics,[45,46] suggesting that synergistic optimization of printing parameters enables sub-millimeter-level control over spheroid size. To monitor the formation and evolution of tumor microspheroids over time, HepG2 and HFL1 were pre-labeled with DiO (green) and DiI (red), respectively (Figure 4D). Under low-adhesion culture conditions, dispersed cells gradually self-assembled into multicellular aggregates and eventually matured into compact tumor microspheroids. As displayed in Figure 4E, the spheroids developed with a defined architecture and initial cell density. Initial total cell density was found to play a key role in spheroid formation. When the cell density reached 5×10^7 cells/mL, dense spheroids formed within only 3 days (Figure 4E). Notably, the low-adhesion culture environment effectively prevented cell migration from the aggregates, thereby ensuring structural

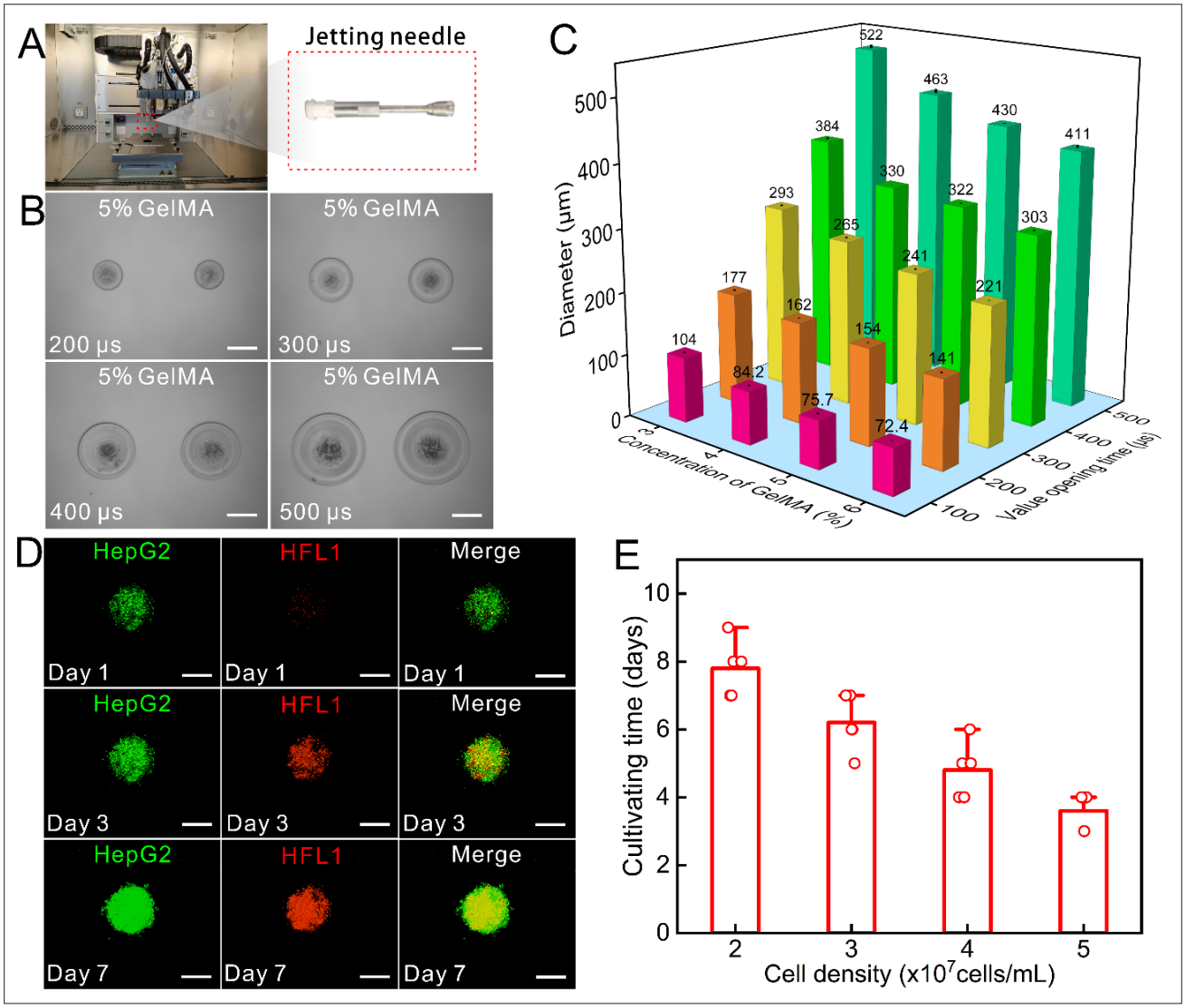

Figure 4. Controlled generation of tumor spheroids via high-precision inkjet bioprinting. (A) Schematic and appearance of the inkjet printing setup; jetting needle (red-dotted box). (B) Size-controlled tumor spheroids printed by varying valve opening times. (C) Statistical chart of initial microspheroid diameters prepared under different printing conditions. (D) Fluorescence images of DiO-labeled HepG2 (green) and DiI-labeled HFL1 (red) aggregating into compact spheroids under low-adhesion conditions. (E) Influence of initial total cell density on spheroid formation dynamics. Experiments were independently repeated at least three times ($n \geq 3$). Scale bars: 200 μm (B and D). Abbreviation: GelMA, Methacrylate Gelatin.

stability and consistent size of the spheroids throughout the subsequent perfusion culture. To further characterize spheroid viability, we performed Calcein-AM/PI staining on tumor spheroids at Days 1, 3, and 7. As presented in Figure S3, Supporting Information, the results demonstrate a progressive formation of a central necrotic core by Day 7—a typical feature of the tumor spheroid architecture that reflects *in vivo* solid tumor physiology.

3.4. Construction and characterization of a multiscale vascularized tumor model

To develop a biomimetic TME model, we first established microvascular networks (prevascular structures formed by HUVECs through self-assembly in a 3D ECM) through the co-culture of HUVECs and HFL1. A matrix composed of 5 mg/mL fibrinogen and 3 mg/mL collagen was used as the extracellular scaffold. Under dynamic perfusion conditions, the co-culture system exhibited robust microvascular formation (Figure 5A). Compared to the HUVEC-only control group, the presence of HFL1 significantly enhanced the elongation and maturation of endothelial cells, likely through VEGF secretion (Figure 5B).[47,48] This observation is consistent with previous studies demonstrating the synergistic role of fibroblasts and endothelial cells in angiogenesis, further supporting the

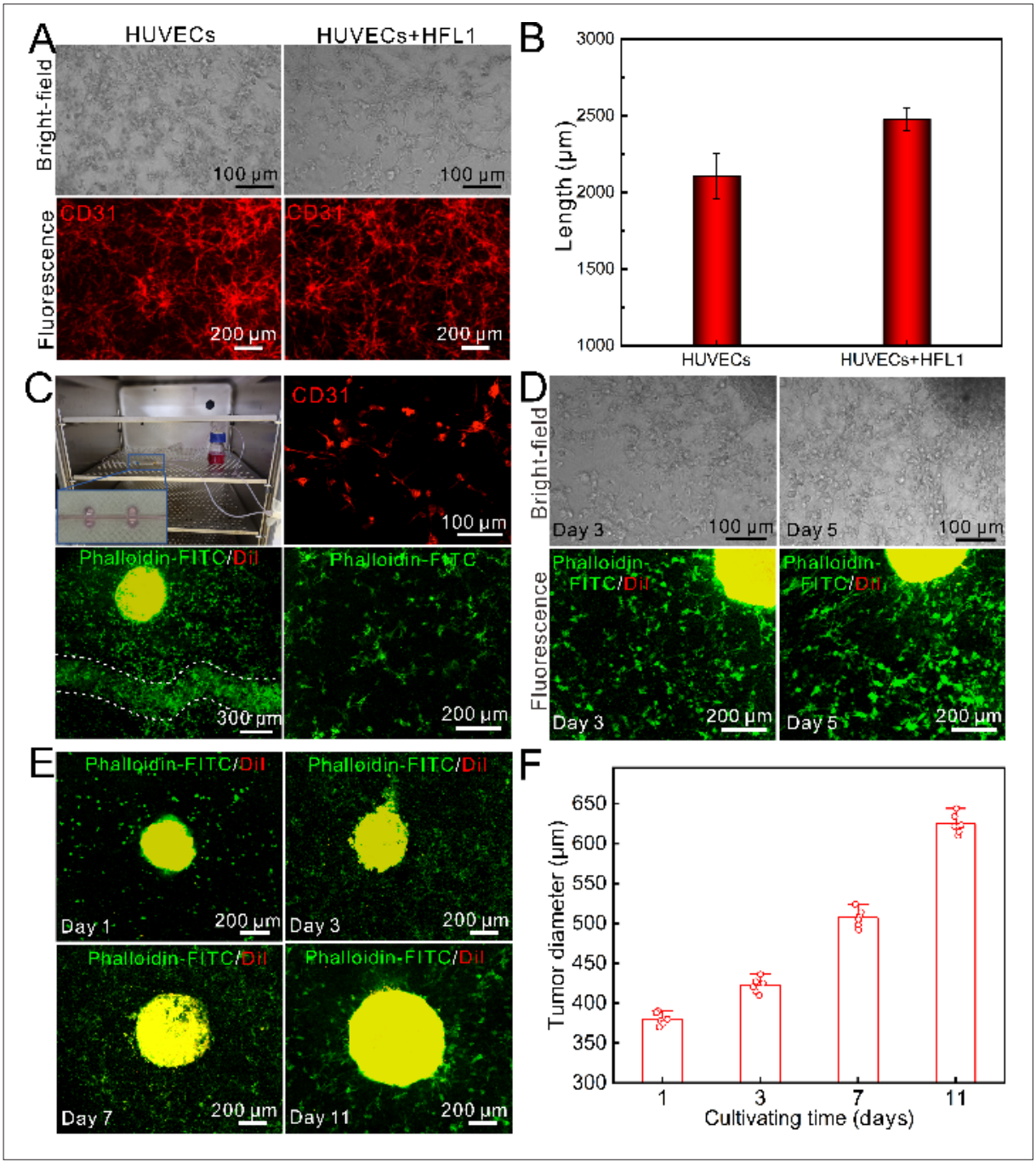

Figure 5. Construction and characterization of the multiscale vascularized tumor model. (A) Comparison of microvascular networks formed with and without HFL1. (B) Quantitative analysis of endothelial elongation in both conditions (i.e., with and without HFL1). (C) Photograph of a multi-level vascularized tumor model cultivation system (C, top-left); fluorescent images of the vascularized tumor region after 7 days of cultivation in the system: CD31 immunofluorescence staining (C, top-right), cellular skeleton staining of the local microvascular network. (D) On Days 3 and 5, bright-field imaging (D, top) and cell skeleton staining (D, bottom) were performed within the perfusion apparatus. (E) Tumor spheroid growth and migration dynamics were tracked under perfusion culture. (F) Quantitative measurement of tumor spheroid size over time. Experiments were independently repeated at least three times ($n \geq 3$). Scale bars: 100 μm (A, top; C, top-right; D, top); 200 μm (A, bottom; C, bottom-right; D, bottom; E); 300 μm (C, bottom-left). Abbreviation: HUVECs, human umbilical vein endothelial cells.

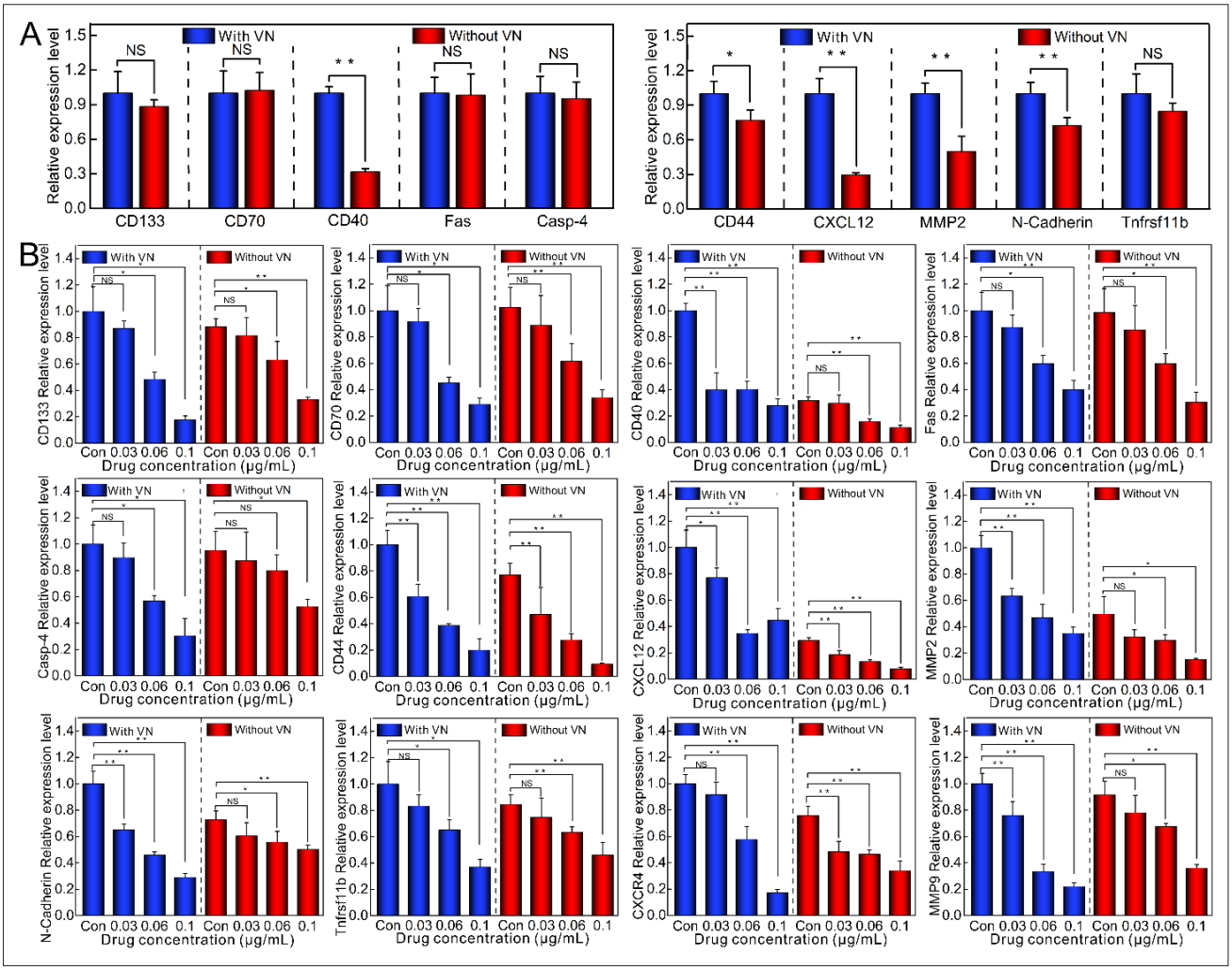

Figure 6. Vascular networks modulate tumor metastasis and drug efficacy in vascularized tumor models. (A) Gene expression levels of markers associated with metastasis and tumor stemness/survival in models with or without vascular networks. (B) Dose-dependent inhibitory effect of paclitaxel on key gene expression, indicating reduced invasiveness and viability in vascularized tumor models. Experiments were independently repeated at least three times ($n \geq 3$). $p < 0.05$, ** for $p < 0.01$, *** for $p < 0.001$, and N.S. for no significant difference. Abbreviations: Con, control; VN, vascular network.

necessity of a co-culture strategy for recapitulating tumor-induced vascularization.[49,50] Building upon the successful generation of microvascular networks, we integrated these with the double-layered vessels and tumor spheroids into a perfusion-compatible chip, resulting in a multiscale vascularized tumor model (Figure 5C). After 3 days of perfusion culture, immunofluorescence staining revealed that CD31-positive endothelial cells and Phalloidin-FITC-stained cytoskeletal structures adopted elongated, physiologically relevant morphologies, indicating active molecular transport capabilities within the microvascular network. By Day 5, radially oriented neovessels emerged around the tumor spheroids (Figure 5D), suggesting that the secretion of growth factors (e.g., VEGF and CXCL12) from the tumor may have induced directional angiogenic sprouting.[51] Furthermore, the tumor spheroids exhibited significant growth under dynamic conditions. The diameter increased from an initial 370 to 620 μm after 11 days of culture (Figure 5E), accompanied by the development of internal metabolic gradients,[52] which may have further stimulated vascular remodeling through hypoxia-induced signaling pathways. Notably, some tumor cells were observed to invade beyond the spheroid boundary in the later stages of culture (Figure 5F), indicating that the model can faithfully recapitulate early tumor invasion behavior, thus offering a visual platform for studying metastatic mechanisms. In addition, during the model design process, we prioritized the use of cell lines that could be co-cultured

under unified culture conditions to ensure stability and consistency. This approach allowed us to establish a robust and reproducible system; however, we acknowledge that it may not fully capture the complexity of the native TME, particularly the diverse phenotypes of tumor-associated fibroblasts. Therefore, this model represents a proof-of-concept framework, which we plan to refine in future studies by incorporating primary cells to enhance physiological relevance. Taken together, these results demonstrate that the multiscale vascularized tumor model not only achieves spatial integration of vascular networks and tumor spheroids but also supports dynamic interactions between the two components. The formation of microvessels is regulated by the synergistic interaction between fibroblasts and endothelial cells, while the tumor spheroids influence vascular morphology through paracrine signaling, forming a bidirectional, biomimetic microenvironment. This model thus serves as a highly representative *in vitro* platform for investigating tumor–vascular crosstalk and evaluating anti-angiogenic therapies.

3.5. Influence of the vascular network on tumor behavior and drug evaluation

To assess the physiological relevance and drug evaluation potential of the multiscale vascularized tumor model, we selected paclitaxel as a model chemotherapeutic agent and investigated the regulatory effects of the vascular network on tumor cell proliferation, metastasis, and drug sensitivity. Quantitative real-time PCR (qRT-PCR) analysis revealed that, in the presence of a vascular network, the expression levels of metastasis-related genes (CD44, CXCL12, MMP2, N-cadherin) and pro-survival genes (CD40) were significantly upregulated compared to those in models lacking vascularization (Figure 6A). The simultaneous upregulation of CD44 and MMP2 suggests that the vascular microenvironment may promote an invasive tumor phenotype by enhancing ECM remodeling.[53] Further dose-dependent experiments with paclitaxel (0.03–0.1 μg/mL) revealed a progressive suppression of these gene expressions (Figure 6B). Specifically, at 0.1 μg/mL paclitaxel, MMP2 and CD44 expression levels decreased to 32% and 28% of the control group, respectively, indicating that the drug effectively inhibited the metastatic potential of tumor cells by disrupting microtubule stability. In addition, Figure S2, Supporting Information demonstrated that the diameter of tumor spheres expanded from ~500 μm on Day 1 to ~750 μm on Day 7, whereas the tumor spheres in the drug-treated group (0.1 μg/mL paclitaxel) exhibited a diameter of only ~650 μm on Day 7, indicating that paclitaxel treatment significantly inhibited the volumetric growth of tumor spheres. These findings confirm that the incorporation of a vascular network within the tumor model significantly modulates tumor cell behavior and enhances the biological relevance of drug response assays. The ability of the model to recapitulate key features of tumor–vascular interactions makes it a powerful tool for evaluating anti-cancer drugs under conditions that more closely mimic *in vivo* tumor physiology.

4. Conclusion

In this study, we successfully developed a multiscale vascularized tumor model by integrating coaxial bioprinting, inkjet printing, and FDM techniques. This model was designed to precisely replicate the dynamic characteristics of the TME, including the mechanical and physiological properties of double-layered vessels, the size controllability of tumor spheroids, and the radial distribution of microvascular networks. Our results demonstrate that the formation of microvessels relies on the synergistic interactions between fibroblasts and endothelial cells, while the tumor spheroids secrete angiogenic factors that induce directional vascular sprouting. This bidirectional crosstalk highlights the model's capability to reproduce critical tumor–vascular interactions. Moreover, drug testing using this platform revealed a concentration-dependent inhibitory effect of paclitaxel on tumor progression, validating the model's potential for preclinical pharmacological screening. Despite these achievements, some limitations remain—including the complexity of fabrication procedures, the lack of immune microenvironment simulation, and challenges in maintaining long-term stability—and the absence of quantitative assessment of endothelial barrier function (e.g., using molecular permeability markers). Future work will aim to enhance the model's biomimicry by incorporating immune components, regulating dynamic oxygen gradients, and incorporating advanced metrics (e.g., fluorescent dextran diffusion or Trans-Epithelial Electrical Resistance [TEER]) to rigorously evaluate physiological transport and endothelial barrier function. Additionally, combining this platform with patient-derived tumor organoids may enable personalized drug sensitivity testing, while single-cell omics technologies could further elucidate the molecular networks underlying tumor-–vascular–immune interactions. Taken together, this study provides a versatile and physiologically relevant *in vitro* platform for the investigation of tumor progression, drug response, and mechanisms of therapy resistance, with broad applications in cancer research and precision medicine.

Acknowledgments

The authors would like to express our gratitude to Tao Ding, Wenqi Wei, and Weihao Teng for their valuable assistance in the preparation of bioink.

Funding

This research was funded by the University Natural Science Research Project of Anhui Province (grant number: 2024AH051533), the Talent Research Foundation of Hefei University (grant number: 21-22RC26), the Natural Science Foundation of Hubei Province (grant number: 2023AFB411), and the Talent Research Foundation of Hefei University (grant number: 20RC40).

Conflict of interest

The authors declare that they have no financial and personal relationships with other people or organizations that can inappropriately influence the study. They also have no professional or other personal interest of any nature or kind in any product, service, and/or company that could be construed as influencing the position presented in, or the review of, the article.

Author contributions

Conceptualization: Jing Liu, Haochen Liu
Formal analysis: Haizhongshi Zhang, Zhenlei Zhang
Investigation: Ying Zhao, Bihan Ren, Jing Liu
Methodology: Dingming Li, Tianma He
Writing–original draft: Jing Liu, Ying Zhao
Writing–review & editing: Haochen Liu

Ethics approval and consent to participate

Not applicable.

Consent for publication

Not applicable.

Availability of data

Data are available from the corresponding author upon reasonable request.

References

1. Lunt N. The global challenge of cancer governance. *World Med Health Pol*. 2023;15(4):672-681.
doi: 10.1002/wmh3.577

2. Sung H, Ferlay J, Siegel RL, et al. Global cancer statistics 2020: GLOBOCAN estimates of incidence and mortality worldwide for 36 cancers in 185 countries. *CA Cancer J Clin*. 2021;71(3):209-249.
doi: 10.3322/caac.21660

3. Sontheimer-Phelps A, Hassell BA, Ingber DE. Modelling cancer in microfluidic human organs-on-chips. *Nat Rev Cancer*. 2019;19(2):65-81.
doi: 10.1038/s41568-018-0104-6

4. Li CP, Li SB, Du K, Li P, Qiu BS, Ding WP. On-chip replication of extremely early-stage tumor behavior. *Acs Appl Mater Inter*. 2021;13(17):19768-19777.
doi: 10.1021/acsami.1c03740

5. Stock K, Estrada MF, Vidic S, et al. Capturing tumor complexity: comparative analysis of 2D and 3D tumor models for drug discovery. *Sci Rep-Uk*. 2016;6:28951.
doi: 10.1038/srep28951

6. Nie J, Gao Q, Fu JZ, He Y. Grafting of 3D bioprinting to in vitro drug screening: a review. *Adv Healthc Mater*. 2020;9(7):e190177310.
doi: 10.1002/adhm.201901773

7. Li JZ, Zhou YJ, Chen WL, et al. A novel 3D in vitro tumor model based on silk fibroin/chitosan scaffolds to mimic the tumor microenvironment. *Acs Appl Mater Inter*. 2018;10(43):36641-36651.
doi: 10.1021/acsami.8b10679

8. Lee G, Kim SJ, Park JK. Fabrication of a self-assembled and vascularized tumor array bioprinting on a microfluidic chip. *Lab Chip*. 2023;23(18):4079-4091.
doi: 10.1039/d3lc00275f

9. Nashimoto Y, Okada R, Hanada S, et al. Vascularized cancer on a chip: the effect of perfusion on growth and drug delivery of tumor spheroid. *Biomaterials*. 2020;229:119547.
doi: 10.1016/j.biomaterials.2019.119547

10. Lee VK, Lanzi AM, Ngo H, Yoo SS, Vincent PA, Dai GH. Generation of multi-scale vascular network system within 3D hydrogel using 3D bio-printing technology. *Cell Mol Bioeng*. 2014;7(3):460-472.
doi: 10.1007/s12195-014-0340-0

11. Eckermann CW, Lehle K, Schmid SA, Wheatley DN, Kunz-Schughart LA. Characterization and modulation of fibroblast/endothelial cell co-cultures for the preformation of three-dimensional tubular networks. *Cell Biol Int*. 2011;35(11):1097-1110.
doi: 10.1042/Cbi20100718

12. Enzerink A, Rantanen V, Vaheri A. Fibroblast nemosis induces angiogenic responses of endothelial cells. *Exp Cell Res*. 2010;316(5):826-835.
doi: 10.1016/j.yexcr.2009.11.012

13. Friedrich J, Ebner R, Kunz-Schughart LA. Experimental anti-tumor therapy in 3-D: spheroids - old hat or new challenge? *Int J Radiat Biol*. 2007;83(11–12):849-871.
doi: 10.1080/09553000701727531

14. Amann A, Zwierzina M, Gamerith G, et al. Development of an Innovative 3D cell culture system to study tumour - stroma interactions in non-small cell lung cancer cells. *Plos One*. 2014;9(3):e92511.
doi: 10.1371/journal.pone.0092511

15. Jing JF, Xiao H, Lin XW, et al. Cutting and Bonding Parafilm® to fast prototyping flexible hanging drop chips for 3d spheroid cultures. *Cell Mol Bioeng*. 2021;14(2):187-199.

doi: 10.1007/s12195-020-00660-x

16. Hurrell T, Ellero AA, Masso ZF, Cromarty AD. Characterization and reproducibility of HepG2 hanging drop spheroids toxicology. *Toxicol in Vitro*. 2018;50:86-94. doi: 10.1016/j.tiv.2018.02.013

17. Meenach SA, Tsoras AN, McGarry RC, Mansour HM, Hilt JZ, Anderson KW. Development of three-dimensional lung multicellular spheroids in air- and liquid-interface culture for the evaluation of anticancer therapeutics. *Int J Oncol*. 2016;48(4):1701-1709. doi: 10.3892/ijo.2016.3376

18. Costa EC, Gaspar VM, Coutinho P, Correia IJ. Optimization of liquid overlay technique to formulate heterogenic 3D co-cultures models. *Biotechnol Bioeng*. 2014;111(8):1672-1685. doi: 10.1002/bit.25210

19. Fennema E, Rivron N, Rouwkema J, van Blitterswijk C, de Boer J. Spheroid culture as a tool for creating 3D complex tissues. *Trends Biotechnol*. 2013;31(2):108-115. doi: 10.1016/j.tibtech.2012.12.003

20. Habanjar O, Diab-Assaf M, Caldefie-Chezet F, Delort L. 3D cell culture systems: tumor application, advantages, and disadvantages. *Int J Mol Sci*. 2021;22(22):12200. doi: 10.3390/ijms222212200

21. Gao W, Wu D, Wang Y, et al. Development of a novel and economical agar-based non-adherent three-dimensional culture method for enrichment of cancer stem-like cells. *Stem Cell Res Ther*. 2018;9(1):243. doi: 10.1186/s13287-018-0987-x

22. Jeong Y, Tin A, Irudayaraj J. Flipped well-plate hanging-drop technique for growing three-dimensional tumors. *Front Bioeng Biotechnol*. 2022;10:898699. doi: 10.3389/fbioe.2022.898699

23. de Barros NR, Gomez A, Ermis M, et al. Gelatin methacryloyl and Laponite bioink for 3D bioprinted organotypic tumor modeling. *Biofabrication*. 2023;15(4):045005. doi: 10.1088/1758-5090/ace0db

24. Wu L, Li H, Liu Y, et al. Research progress of 3D-bioprinted functional pancreas and in vitro tumor models. *Int J Bioprint*. 2024;10(1):1256. doi: 10.36922/ijb.1256

25. Singh S, Ray LA, Shahi Thakuri P, et al. Organotypic breast tumor model elucidates dynamic remodeling of tumor microenvironment. *Biomaterials*. 2020;238:119853. doi: 10.1016/j.biomaterials.2020.119853

26. Zhou X, Nowicki M, Sun H, et al. 3D bioprinting-tunable small-diameter blood vessels with biomimetic biphasic cell layers. *ACS Appl Mater Inter*. 2020;12(41):45904-45915. doi: 10.1021/acsami.0c14871

27. Meng FB, Meyer CM, Joung D, Vallera DA, McAlpine MC, Panoskaltsis-Mortari A. 3D bioprinted in vitro metastatic models via reconstruction of tumor microenvironments. *Adv Mater*. 2019;31(10):1806899. doi: 10.1002/adma.201806899

28. Nie J, Gao Q, Xie CQ, et al. Construction of multi-scale vascular chips and modelling of the interaction between tumours and blood vessels. *Mater Horizons*. 2020;7(1):82-92. doi: 10.1039/c9mh01283d

29. Gao G, Kim H, Kim BS, et al. Tissue-engineering of vascular grafts containing endothelium and smooth-muscle using triple-coaxial cell printing. *Appl Phys Rev*. 2019;6(4):041402. doi: 10.1063/1.5099306

30. Duong V, Dang TT, Hwang CH, Back SH, Koo KI. Coaxial printing of double-layered and free-standing blood vessel analogues without ultraviolet illumination for high-volume vascularised tissue. *Biofabrication*. 2020;12(4): 045033. doi: 10.1088/1758-5090/abafc6

31. Kwak TJ, Lee E. In vitro modeling of solid tumor interactions with perfused blood vessels. *Sci Rep-Uk*. 2020;10(1): 20142. doi: 10.1038/s41598-020-77180-1

32. Ahn J, Kim D, Koo DJ, et al. 3D microengineered vascularized tumor spheroids for drug delivery and efficacy testing. *Acta Biomater*. 2023;165:153-167. doi: 10.1016/j.actbio.2022.10.009

33. Dey M, Kim MH, Dogan M, et al. Chemotherapeutics and CAR-T cell-based immunotherapeutics screening on a 3D bioprinted vascularized breast tumor model. *Adv Funct Mater*. 2022;32(52):2203966. doi: 10.1002/adfm.202203966

34. Ozturk MS, Lee VK, Zou HY, Friedel RH, Intes X, Dai GH. High-resolution tomographic analysis of in vitro 3D glioblastoma tumor model under long-term drug treatment. *Sci Adv*. 2020;6(10):eaay7513. doi: 10.1126/sciadv.aay7513

35. Hwang DG, Choi YM, Jang J. 3D bioprinting-based vascularized tissue models mimicking tissue-specific architecture and pathophysiology for studies. *Front Bioeng Biotech*. 2021;9:685507. doi: 10.3389/fbioe.2021.685507

36. Nashimoto Y, Hayashi T, Kunita I, et al. Integrating perfusable vascular networks with a three-dimensional tissue in a microfluidic device. *Integr Biol-Uk*. 2017;9(6):506-518. doi: 10.1039/c7ib00024c

37. Velez C, Cheng K, Crosby C. Synthesis and Characterization of Gelatin Methacryloyl: Introducing Chemistry Students to the Applications of Hydrogels in Medicine. *J Chem Educ*. 2024;101(3):1171-1179. doi: 10.26434/chemrxiv-2023-qbrh6

38. Millik SC, Dostie AM, Karis DG, et al. 3D printed coaxial nozzles for the extrusion of hydrogel tubes toward modeling vascular endothelium. *Biofabrication*. 2019;11(4):045009. doi: 10.1088/1758-5090/ab2b4d

39. Siminska-Stanny J, Nicolas L, Chafai A, et al. Advanced PEG-tyramine biomaterial ink for precision engineering of perfusable and flexible small-diameter vascular constructs

via coaxial printing. *Bioact Mater*. 2024;36:168-184.
doi: 10.1016/j.bioactmat.2024.02.019

40. Elliott MB, Gerecht S. Three-dimensional culture of small-diameter vascular grafts. *J Mater Chem B*. 2016;4(20):3443-3453.
doi: 10.1039/c6tb00024j

41. Xia Y, Zhou HY, Ou JS, Liu YQ. The potential of a new natural vessel source: decellularized intercostal arteries as sufficiently long small-diameter vascular grafts. *Bioengineering (Basel)*. 2024;11(7): 700.
doi: 10.3390/bioengineering11070700

42. Carrabba M, Fagnano M, Ghorbel MT, et al. Development of a novel hierarchically biofabricated blood vessel mimic decorated with three vascular cell populations for the reconstruction of small-diameter arteries. *Adv Funct Mater*. 2024;34(7):adfm.202300621.
doi: 10.1002/adfm.202300621

43. Haase K, Offeddu GS, Gillrie MR, Kamm RD. Endothelial regulation of drug transport in a 3D vascularized tumor model. *Adv Funct Mater*. 2020;30(48):2002444.
doi: 10.1002/adfm.202002444

44. Marei I, Abu Samaan T, Al-Quradaghi MA, et al. 3D tissue-engineered vascular drug screening platforms: promise and considerations. *Front Cardiovasc Med*. 2022;9:847554.
doi: 10.3389/fcvm.2022.847554

45. Ma DF, Liang D, Zhu CY, et al. The breakup dynamics and mechanism of viscous droplets in Y-shaped microchannels. *Chem Eng Sci*. 2021;231:116300.
doi: 10.1016/j.ces.2020.116300

46. Sur S, Rothstein J. Drop breakup dynamics of dilute polymer solutions: effect of molecular weight, concentration, and viscosity. *J Rheol*. 2018;62(5):1245-1259.
doi: 10.1122/1.5038000

47. Cho WJ, Elbasiony E, Singh A, Mittal SK, Chauhan SK. IL-36 gamma augments ocular angiogenesis by promoting the vascular endothelial growth factor-vascular endothelial growth factor receptor axis. *Am J Pathol*. 2023;193(11):1740-1749.
doi: 10.1016/j.ajpath.2023.01.003

48. Sitohy B, Chang S, Sciuto TE, et al. Early actions of anti-vascular endothelial growth factor/vascular endothelial growth factor receptor drugs on angiogenic blood vessels. *Am J Pathol*. 2017;187(10):2337-2347.
doi: 10.1016/j.ajpath.2017.06.010

49. Truelsen SLB, Mousavi N, Wei HC, et al. The cancer angiogenesis co-culture assay: quantification of the angiogenic potential of tumoroids. *Plos One*. 2021;16(7):e0253258.
doi: 10.1371/journal.pone.0253258

50. Rodoplu D, Matahum JS, Hsu CH. A microfluidic hanging drop-based spheroid co-culture platform for probing tumor angiogenesis. *Lab Chip*. 2022;22(7):1275-1285.
doi: 10.1039/d1lc01177d

51. Chang CW, Seibel AJ, Avendano A, Cortes-Medina MG, Song JW. Distinguishing specific CXCL12 isoforms on their angiogenesis and vascular permeability promoting properties. *Adv Healthc Mater*. 2020;9(4):e1901399.
doi: 10.1002/adhm.201901399

52. Zhou L, Wang L, Song X, Zhang X, Xiao Y. A tetrazine-based ratiometric sensor quantifying ph gradient in tumorspheres through bio-orthogonal labeling. *Anal Chem*. 2025;97(22):11486-11495.
doi: 10.1021/acs.analchem.5c00291

53. Lee S, Park J, Cho S, et al. Hyaluronan network remodeling by ZEB1 and ITIH2 enhances the motility and invasiveness of cancer cells. *J Clin Invest*. 2025;135(11):e180570.
doi: 10.1172/JCI180570